Mass models of the Milky Way

Walter Dehnen and James Binney

Theoretical Physics, 1 Keble Road, Oxford OX1 3NP

ABSTRACT

A parametrized model of the mass distribution within the Milky Way is fitted to the available observational constraints. The most important single parameter is the ratio of the scalelength $R_{d,*}$ of the stellar disc to R_0. The disc and bulge dominate $v_c(R)$ at $R \lesssim R_0$ only for $R_{d,*}/R_0 \lesssim 0.3$. Since the only knowledge we have of the halo derives from studies like the present one, we allow it to contribute to the density at all radii. When allowed this freedom, however, the halo causes changes in assumptions relating to $R \ll R_0$ to affect profoundly the structure of the best-fitting model at $R \gg R_0$. For example, changing the disc slightly from an exponential surface-density profile significantly changes the form of $v_c(R)$ at $R \gg R_0$, where the disc makes a negligible contribution to v_c. Moreover, minor changes in the constraints can cause the halo to develop a deep hole at its centre that is not physically plausible. These problems call into question the proposition that flat rotation curves arise because galaxies have physically distinct haloes rather than outwards-increasing mass-to-light ratios.

The mass distribution of the Galaxy and the relative importance of its various components will remain very uncertain until more observational data can be used to constrain mass models. Data that constrain the Galactic force field at $z \gtrsim R$ and at $R > R_0$ are especially important.

Key words: Galaxy: kinematics and dynamics – Galaxy: structure.

1 INTRODUCTION

One of the fundamental tasks of Galactic astronomy is the determination of the mass and luminosity distributions of the Milky Way. In the 1950s the development of radio astronomy opened up the study of the large-scale structure of the Galaxy, and much of the understanding that was attained at that time was summarized by Schmidt's (1956) mass model. In the 1970s and early 1980s our picture of the Milky Way changed in response both to studies of external galaxies and to a growing awareness of the existence of 'dark matter' at large radii. These developments were reflected in the Bahcall & Soneira (1980), Caldwell & Ostriker (1981) and Rohlfs & Kreitschmann (1988) Galaxy models. These models were based on two rather different methodologies: whereas Bahcall & Soneira concentrated on fitting the distribution of *luminosity* within the Galaxy by fitting star counts, Caldwell & Ostriker and Rohlfs & Kreitschmann concentrated on fitting various measures of the Galactic gravitational force-field. Nevertheless, all these models decompose the Galaxy into 'components' that are motivated by photometric studies of external galaxies, and incorporated a range of dynamical constraints. It is our aim in this and subsequent papers to update and extend these models.

The principal direction in which we wish to extend traditional galaxy models is the incorporation of kinematic information that is capable of constraining the degree of flattening of the mass distribution. The kinematic information that has traditionally been used to constrain galaxy models – the shape of the circular-speed curve, the values of the Oort constants, etc. – relates almost exclusively to the radial force within the plane. Such information is in principle incapable of determining how much of the Galaxy's mass lies near the plane, which is clearly of prime importance astrophysically.

This deficit of kinematic information has been papered over in two ways. The first is a one-dimensional analysis of the vertical structure of the disc along the lines pioneered by Oort (1932). Such analyses ultimately come up against the problem that the vertical and horizontal motions of stars do not decouple to the necessary degree, so that a one-dimensional analysis cannot precisely determine the vertical distribution of matter – see, e.g., Kuijken & Gilmore (1991).

The second way in which the deficit of kinematic constraints on the vertical structure of the Galaxy has been papered over is to use star counts to constrain the flattening of the components into which the overall luminosity density is decomposed, and to assume that each component i is characterized by a constant mass-to-light ratio Υ_i. This procedure is methodologically questionable since it appears to presume that the phenomenon of 'dark matter' implies the existence of a completely dark component comprised of exotic particles, whereas it may merely reflect the variation from point to point of each Υ_i.

This is the first of a series of papers in which we plan to overcome these difficulties by treating the orbits of stars in the meridional plane with sufficient sophistication. Our approach, which has been described elsewhere (Binney 1994; Dehnen & Binney 1996), is

iterative: we choose a potential, determine a range of orbits in this potential, populate these with stars of various spectral types and then compare the resulting predictions with the available surveys. The potential is modified in the light of this comparison. Thus our first step is to choose potentials (and thus, implicitly, mass models) that are compatible with all the standard kinematic and photometric constraints. This task of updating the Caldwell & Ostriker and Rohlfs & Kreitschmann models is even now by no means trivial, as is made apparent by recent divergent results (Gates, Gyuk & Turner 1995; Cowsik, Ratnam & Bhattacharjee 1996; Evans 1996). Therefore we believe it will be useful to present in this paper our initial mass models and consider the actions upon which they are based. Computer programs for evaluating the density and potential of the models are available upon request to the authors. Although there is now abundant evidence that the inner Galaxy is significantly non-axisymmetric, our model conforms to the traditional axisymmetric pattern because the success of axisymmetric models in accounting for observations in the 21-cm line of hydrogen at longitudes $l \gtrsim 30°$ suggests that orbits in the Galactic potential that carry stars to radii $r \gtrsim 5$ kpc can be accurately modelled by orbits in an axisymmetric potential.

We do not distinguish between the visible halo, of which RR Lyrae stars and metal-poor globular clusters are classical tracers, and the putative dark halo: since we do not understand why the mass-to-light ratio rises with Galactocentric radius r, we are at liberty to assume that the Galaxy possesses a single, massive halo that simply becomes more luminous with decreasing r.

2   FUNCTIONAL FORMS

Our mass model contains three principal components: the disc, the bulge and the halo.

2.1   The disc

Our disc is made up of three components, namely the interstellar medium (ISM), and the thin and thick stellar discs. The density of each sub-disc is given by

$$\rho_d(R, z) = \frac{\Sigma_d}{2z_d} \exp\left(-\frac{R_m}{R_d} - \frac{R}{R_d} - \frac{|z|}{z_d}\right), \tag{1}$$

With $R_m = 0$, equation (1) describes a standard double exponential disc with scalelength R_d, scaleheight z_d and central surface-density Σ_d. Since there appears to be very little interstellar gas between the molecular ring at $R = 4$–5 kpc and the nuclear disc at $\lesssim 200$ pc (Dame et al. 1987), there should be a depression in the central surface-density of the ISM. The parameter R_m in equation (1) allows for such a central depression. We set $R_m = 0$ for the stellar discs and adopt $R_m = 4$ kpc for the ISM. The total mass of a disc with density (1) is

$$M_d = 4\pi \Sigma_d R_m R_d K_2(2\sqrt{R_m/R_d}), \tag{2}$$

where K_2 is a modified Bessel function. For $R_m = 0$ this gives $M_d = 2\pi\Sigma_d R_d^2$.

Table 1 gives our adopted values of the scaleheights of the three sub-discs as well as the fraction of the surface density of the whole disc at R_0 which is contributed by each sub-disc. As can also be seen from this table, we fix the ratios between the scalelengths of the sub-disc. The value of R_d, the scalelength of the stellar disc, and the mass of the whole disc are obtained from least-squared fits to the observational constraints to be discussed below.

Table 1. Fixed parameters of the disc components.

Component	Contribution to $\Sigma(R_0)$	R_d/R_d, *	R_m	z_d
ISM	0.25	2	4 kpc	40 pc
thin disc	0.70	1	0	180 pc
thick disc	0.05	1	0	1000 pc

2.2   Bulge and halo

The bulge and halo are each described by the spheroidal density distribution

$$\rho_s = \rho_0 \left(\frac{m}{r_0}\right)^{-\gamma} \left(1 + \frac{m}{r_0}\right)^{\gamma - \beta} e^{-m^2/r_t^2}, \tag{3}$$

where

$$m \equiv (R^2 + q^{-2}z^2)^{1/2}. \tag{4}$$

Thus the density of bulge and halo is proportional to $r^{-\gamma}$ for $r \ll r_0$, proportional to $r^{-\beta}$ for $r_0 \ll r \ll r_c$, and is softly truncated at $r = r_t$. Infrared photometry obtained by the *COBE/DIRBE* satellite and analysed by Spergel (private communication) yields values for four of the five bulge parameters: we adopt $\beta_b = \gamma_b = 1.8$, $q_b = 0.6$, $r_{0,b} = 1$ kpc, and $r_{t,b} = 1.9$ kpc. The density normalization $\rho_{0,b}$, which is not determined by the *COBE/DIRBE* data, is obtained from our least-squared fits.

The axial ratio of the halo is not significantly constrained by the observations discussed below, and we arbitrarily set it to $q_h = 0.8$ (our standard value). However, we will also consider models with $q_h = 0.3$ motivated by (i) possible evidence that the haloes of external galaxies might be that flat (Olling 1996; Sackett et al. 1994), and (ii) Sciama's (1990) decaying neutrino model for dark matter that requires a high local neutrino density ($\sim 0.04\,\mathrm{M_\odot\,pc^{-2}}$) only achievable with a flat neutrino halo.

The remaining five halo parameters, β_h, γ_h, $\rho_{0,h}$, $r_{0,h}$, and $r_{t,h}$, are determined by the least-squares fitting procedure described below subject to the restrictions $-2 \leq \gamma_h \leq \gamma_b$ and $\beta_h \geq 1$, which limit the sharpness of any inner and outer edges of the halo, respectively.

2.3   Gravitational potential and forces

The total gravitational potential Φ of a model must satisfy Poisson's equation

$$\frac{\nabla^2\Phi}{4\pi G} = \sum_{j=1}^{2} \rho_{s,j} + \sum_{i=1}^{3} \rho_{d,i}. \tag{5}$$

A standard way to solve (5) involves expanding ρ in spherical harmonics (cf. Binney & Tremaine 1987, section 2.8). Unfortunately, the expansion of a thin disc converges very slowly, so this straightforward approach does not yield a fast and accurate solution of Poisson's equation.

Fortunately, Kuijken & Dubinski (1994) have described a modified multipole technique that works well when the density is sum over components that are separable in cylindrical coordinates, that is, are of the form

$$\rho_{d,i} = f_i(R)\,h_i(z), \tag{6}$$

where $1 = \int_{-\infty}^{\infty} h_i\,dz$ so that $f(R)$ is the radial surface-density profile. Let $H_i(z)$ be such that

(i) $H_i''(z) \equiv h_i(z)$ and

(ii) $H_i(0) = H_i'(0) = 0,$ (7)

Table 2. Pairs of functions $h(z)$ and $H(z)$ defined in Section 2.3.

$h(z) \equiv \mathrm{d}^2 H/\mathrm{d}z^2$	$H(z)$
$\delta(z)$	$\dfrac{|z|}{2}$
$\dfrac{1}{2z_d} \exp\left(-\dfrac{|z|}{z_d}\right)$	$\dfrac{z_d}{2}\left[\exp\left(-\dfrac{|z|}{z_d}\right) - 1 + \dfrac{|z|}{z_d}\right]$
$\dfrac{1}{4z_d} \operatorname{sech}^2 \dfrac{z}{2z_d}$	$z_d \ln \cosh \dfrac{z}{2z_d}$

where the prime denotes a derivative as usual. Then we write

$$\Phi(R,z) = \Phi_{\mathrm{ME}}(R,z) + 4\pi G \sum_i f_i(r) H_i(z), \tag{8}$$

where the argument of f_i is now the spherical radius r rather than the cylindrical radius R and Φ_{ME} is a function to be determined. At $z = 0$ the second term on the right-hand side of (8) and its first derivatives vanish, so both the potential and the forces in the plane are determined by Φ_{ME} alone. Inserting (6) and (8) into (5) we obtain for Φ_{ME}

$$\frac{\nabla^2 \Phi_{\mathrm{ME}}}{4\pi G} = \sum_j \rho_{s,j} + \sum_i \left\{ \left[f_i(R) - f_i(r) \right] h_i(z) \right.$$
$$\left. - f_i''(r) H_i(z) - \frac{2}{r} f_i'(r) \left[H_i(z) + z H_i'(z) \right] \right\}. \tag{9}$$

This equation takes the form of Poisson's equation for Φ_{ME} with a mass-density given by the complex expression on its right-hand side. At $z = 0$ we have $R = r$, so with (7) this expression simplifies to $\sum_j \rho_{s,j}$. That is, Φ_{ME} is generated by a mass distribution that is not strongly confined to the plane, and can be economically evaluated by expanding both sides of equation (9) in spherical harmonics.

Once Φ_{ME} has been found, it and its first derivatives are stored on a grid in $\ln r$ and $|z/r|$. A two-dimensional fifth-order spline is used to interpolate on this grid: at each grid point this spline yields the stored values of the potential and its derivatives, and the forces have everywhere continuous first and second derivatives. In particular, the interpolated forces agree with the derivatives of the interpolated potential, as is necessary if energy is to be accurately conserved along numerically integrated orbits. Furthermore, the evaluation of potential and forces is quick once the spline coefficients have been computed.

We plan to make available after publication of this paper a c++ source code for the evaluation of the potential of any superposition of spheroids (equation 3) and exponential discs with vertical profiles as in Table 2 – send e-mail to w.dehnen@physics.ox.ac.uk. (Public-domain c compilers are available that allow c++ code to be linked to otherwise pure c programs.)

3 THE OBSERVATIONAL CONSTRAINTS

Three groups of observational data constrain the values of the free parameters in the model introduced in Section 2: (i) tangent velocities at $R < R_0$; (ii) rotation velocities at $R > R_0$; (iii) other data, such as the values of Oort's constants and the local surface density. We discuss each group of constraints separately.

3.1 Terminal velocities for the inner Galaxy

For an axisymmetric Galaxy with circularly rotating ISM, the peak velocity along a given line-of-sight at $b = 0$ and l in either the first or fourth quadrant originates from the radius $R = R_0 \sin l$. Relative to the local standard of rest (LSR) this 'terminal velocity' is related to the circular speed v_c by

$$v_{\mathrm{term}} = v_c(R_0 \sin l) - v_c(R_0) \sin l. \tag{10}$$

In reality, non-circular motions of the ISM induced, for instance, by spiral arms, lead to deviations from this ideal relation. However, outside the region $|l| \lesssim 20°$ that is dominated by the bar, these deviations are expected to be ignorable for our purposes.

Numerous surveys of the ISM have been undertaken. In this study we restrict ourselves to three surveys in H I (Weaver & Williams 1973; Bania & Lockman 1984; Kerr et al. 1986) and one in CO (Knapp, Stark & Wilson 1985). Malhotra (1994, 1995) has modelled these raw data in detail and kindly provided us with her values for the terminal velocities in electronically readable form. We restrict the data to $|\sin l| \geq 0.3$ to avoid distortions by the central bar.

3.2 The rotation curve of the outer Galaxy

For an axisymmetric galaxy, the radial velocity relative to the LSR, v_{lsr}, of a circularly orbiting object at galactic coordinates (l, b) and galactocentric radius R is related to the circular speed by

$$W(R) \equiv \frac{v_{\mathrm{lsr}}}{\sin l \cos b} = \frac{R_0}{R} v_c(R) - v_c(R_0). \tag{11}$$

As is well known, for $R > R_0$ one cannot infer R for an object at given l without a knowledge of the distance d to the object. If d is known, then R follows from

$$R = \left(d^2 \cos^2 b + R_0^2 - 2R_0 d \cos b \cos l \right)^{1/2}. \tag{12}$$

Several studies are available that contain measured values of W and d for objects that ought to be on nearly circular orbits. Here we use the data of two recent studies. Brand & Blitz (1993) list H II regions/reflection nebulae that have (spectro-) photometric distances and associated molecular clouds with measured radial velocities. Pont et al. (1997) give radial velocities and photometry for classical Cepheids in the outer disc. For these objects we have transformed v_r to v_{lsr} and evaluated the distances using the period–luminosity relation derived from *Hipparcos* parallaxes by Feast and co-workers (Feast & Catchpole 1997; Feast & Whitelock 1997), $M_V = -2.81 \log P - 1.43$, in conjunction with a Galactic period–colour relation from Laney & Stobie (1994): $(B - V)_0 = 0.416 \log P + 0.314$.

We have rejected objects for which either $155° \leq l \leq 205°$, or $d < 1$ kpc, or $W > 0$, because for these objects v_{lsr} is very likely dominated by non-circular motions. Furthermore, we have not used data points at $R < R_0$ where the terminal velocities provide a much better constraint. 93 of the 205 objects in Brand & Blitz (1993) and 26 of the 48 Cepheids survived this cull.

We have not employed a number of data sets that are similar in scope to those of Brand & Blitz and Pont et al. because these sets are either rather restricted in their radial coverage, or have problematic distances. For example, the distances to carbon stars are seriously affected by both Malmquist bias and interstellar extinction (Schechter, private communication).

A technique for measuring $W(R)$ from 21-cm emission without independent distance information has been proposed by Merrifield (1992). This involves a determination of the extent in b of the emission observed at given W: in an axisymmetric galaxy with circularly orbiting H I, all emission at a given W will originate in a
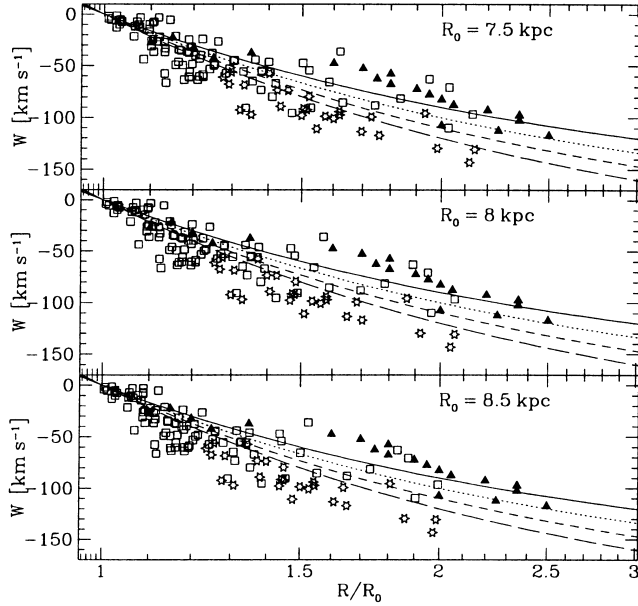
Figure 1. Data on the outer rotation curve: W versus R/R_0 (errorbars are omitted for clarity). Squares, stars, and triangles represent H II regions, Cepheids, and H I measurements, respectively. The lines refer to flat rotation curves with $v_c(R_0) = 180$ km s^{-1} (solid), 200 km s^{-1} (dotted), 220 km s^{-1} (short dashed) and 240 km s^{-1} (long dashed), respectively. Each panel corresponds to a different assumed value of R_0; increasing R_0 shifts the squares and the stars to the left.

galactocentric ring. If this ring has a constant vertical extension, it creates a distinct pattern in the (l, b) plane. From the H I surveys of Weaver & Williams (1974) and Kerr et al. (1986) Merrifield estimated relative galactocentric distances R/R_0 by fitting this characteristic pattern to the emission from each bin in W. It is not immediately apparent how accurate Merrifield's radii are since both random motions in the plane and systematic variations in the thickness of the H I layer around circles will contribute errors.

It is worth comparing the three data sets before trying to fit them to a mass model. Fig. 1 shows the data in W versus R/R_0 for $R_0 = 7.5$, 8 and 8.5 kpc. Also shown is $W(R)$ predicted by flat rotation curves for $v_c(R_0) = 180$ (uppermost line), 200, 220 and 240 km s^{-1} (lowest line). Several points can be drawn immediately from this figure. (i) The data of Merrifield (using H I) at $R > 1.3R_0$ are incompatible with the Cepheid data (Pont et al. 1997). (ii) The H II data at $R < 1.5R_0$ and the Cepheid data imply a falling rotation curve, unless $v_c(R_0) \gtrsim 240$ km s^{-1} and/or $R_0 \lesssim 7.5$ kpc. (iii) Merrifield's measurements require a rising rotation curve, unless $v_c(R_0) \lesssim 180$ km s^{-1}.

Clearly, it makes no sense trying to fit inconsistent data; we must decide which data to trust. Cepheid distances have been extensively studied, whereas Merrifield's novel method rests on several ad hoc assumptions. Furthermore, his values for W are suspect because they are non-monotonic at $R > 2R_0$. (Note that they do not represent individual objects as do the other data points.) Therefore, we have decided to discard Merrifield's points altogether.

3.3 Other constraints

By dividing equation (10) by $R_0 \sin l$ and equation (11) by R_0, one sees that studies of the ISM measure $\Omega \equiv v_c(R)/R$ at various positions in the Milky Way *relative* to its local value. To fix the *absolute* values of v_c, additional information is essential.

3.3.1 Oort's constants

Oort's constants A and B are defined by

$$A = \frac{1}{2}\left(\frac{v_c}{R} - \frac{\partial v_c}{\partial R}\right)$$
$$B = -\frac{1}{2}\left(\frac{v_c}{R} + \frac{\partial v_c}{\partial R}\right). \tag{13}$$

They can be derived from the kinematics of nearby stars. Kerr & Lynden-Bell (1986) reviewed the published measurements and concluded that $A = 14.4 \pm 1.2$, $B = -12.0 \pm 2.8$, and $A - B = 26.4 \pm 1.9$, all in units of km s^{-1} kpc^{-1}. Hanson (1987) found from an analysis of the NPM catalogue $A = 11.3 \pm 1.1$, $B = -13.9 \pm 0.9$, and $A - B = 25.2 \pm 1.6$, while a more recent study of *Hipparcos* proper motions for Cepheids by Feast & Whitelock (1997) yields $A = 14.8 \pm 0.8$, and $A - B = 27.2 \pm 0.9$ in the same units. Since the *Hipparcos* values are likely to be significantly more reliable than the earlier studies, we give them the highest weight.

A potentially relevant measurement is of the proper motion of Sgr A*: $\mu_l = (-6.55 \pm 0.17)$ mas yr^{-1} $= (-31.05 \pm 0.81)$ km s^{-1} kpc^{-1} (Backer 1996). To this the peculiar motion of the Sun contributes $V_\odot/R_0 \simeq 1$ km s^{-1} kpc^{-1}. Hence, if we believe that Sgr A*, which is certainly massive (Eckart & Genzel 1997), is stationary at the centre of the Galaxy then we have $A - B = 30 \pm 1$ km s^{-1} kpc^{-1}, which is significantly inconsistent with the result of Feast & Whitelock. In view of this conflict and the possibility that the Galactic Centre is oscillating, perhaps in an $m = 1$ mode, (Gould & Ramírez 1997) we have not used Backer's result but imposed the constraints[1]

$$
\begin{aligned}
A &= 14.5 &\pm 1.5 &\quad \text{km s}^{-1}\text{ kpc}^{-1} \\
B &= -12.5 &\pm 2 &\quad \text{km s}^{-1}\text{ kpc}^{-1} \\
A - B &= 27 &\pm 1.5 &\quad \text{km s}^{-1}\text{ kpc}^{-1}.
\end{aligned} \tag{14}
$$

3.3.2 The mass at large radii

While observations for A, B, and $v_c(R_0)$ restrict the circular speed locally, and hence the mass inside R_0, there are some important constraints at much larger radii. The total mass within a sphere of radius $r \gg R_0$ can be estimated (i) from the velocity distribution of the Milky Way's satellites, (ii) from the maximal locally observed stellar velocity (the 'escape velocity' argument), (iii) the timing of the local group, and (iv) by modelling the dynamics of the Magellanic Clouds and Stream. All these estimates rely on certain assumptions and are model dependent. However, with reasonable assumptions Kochanek (1996) found a simple model that satisfies the first three of these constraints and yields an acceptable value of $v_c(R_0)$. From his fig. 7 we extracted for the mass inside 100 kpc $M_{R<100\,\text{kpc}} = 7.5 \pm 2 \times 10^{11}$ M$_\odot$. For comparison, by modelling the dynamics of the Magellanic Clouds and Stream, Lin, Jones & Klemola (1995) found that $M_{R<100\,\text{kpc}} = 5.5 \pm 1 \times 10^{11}$ M$_\odot$. Clearly, the uncertainties here are dominated by systematic errors, so we allow for a generous error bound on our adopted constraint, which is

$$M_{R<100\,\text{kpc}} = (7 \pm 2.5) \times 10^{11} \text{ M}_\odot. \tag{15}$$

---

[1] The product AR_0 is not an independent observable, as it is usually measured from the terminal velocities of the ISM, which have already been employed as constraints.

3.3.3 The local vertical force

The vertical force K_z at some height above the plane places a condition on the local mass distribution, and certainly is an important observable our model must agree with. Using K stars as a tracer population, Kuijken & Gilmore (1989,1991) have deduced

$$K_{z_{1.1}} \equiv |K_z(R_0, 1.1\,\text{kpc})| = 2\pi\,G \times (71 \pm 6)\,\text{M}_\odot\,\text{pc}^{-2}. \quad (16)$$

We have adopted this as a constraint for our models.

3.3.4 The local surface density of the disc

Unfortunately, the local disc surface density Σ_0 is not as well determined as the closely related quantity $K_{z_{1.1}}$ (Kuijken & Gilmore 1991). However, by counting identified matter Kuijken & Gilmore (1989) concluded that $\Sigma_{\text{stars+gas}}(R_0) = 48 \pm 8$ M$_\odot$ pc^{-2}. We adopt the constraint

$$\Sigma_0 \equiv \Sigma_{\text{disc}}(R_0) \gtrsim 40\ \text{M}_\odot\,\text{pc}^{-2}. \quad (17)$$

3.3.5 The dispersion velocity in Baade's window

Finally, an important constraint on the bulge is provided by the observed velocity dispersion of the bulge in Baade's window of $117 \pm 5\,\text{km s}^{-1}$ (Rich 1988; Terndrup, Sadler & Rich 1995). The simplest way to estimate the velocity dispersion of our models is to solve the Jeans equations assuming isotropy in the velocities, which yields

$$\sigma_{\text{b}}^2 = \frac{1}{\rho_{\text{b}}} \int_z^\infty \rho_{\text{b}}\,\frac{\partial \Phi}{\partial z}\,\text{d}z, \quad (18)$$

where the subscript b stands for bulge. The bulge is now known to be significantly elongated towards us (e.g., Binney, Gerhard & Spergel 1997) and this elongation is probably reflected in the line-of-sight dispersion along the minor axis of the Galaxy being larger than equation (18) allows. On the other hand, the velocity dispersion probably falls as one moves away from the minor axis along the line of sight, and this effect will tend to cause equation (18) to over-estimate the measured dispersion within Baade's window. In view of these oppositely directed factors, we adopt (18) as the central value of our constraint on the dispersion within Baade's window and allow a wide range around this value:

$$\sigma_{\text{BW}} \equiv \sigma_{\text{b}}(0.0175R_0, -0.068R_0) = 117 \pm 15\,\text{km s}^{-1}. \quad (19)$$

4 FITTING THE MASS MODEL

The free parameters of the mass model described in Section 2 are determined by minimizing the quantity

$$\chi_{\text{tot}}^2 = \frac{W_{\text{in}}}{N_{\text{in}}}\chi_{\text{in}}^2 + \frac{W_{\text{out}}}{N_{\text{out}}}\chi_{\text{out}}^2 + \frac{W_{\text{other}}}{N_{\text{other}}}\chi_{\text{other}}^2, \quad (20)$$

that is the sum of pseudo-chi-squared contributions from our three classes of constraint. Here the N_i are the numbers of data points actually used, while the W_i are weights, which may be interpreted as the number of really independent constraints (for instance, Oort's A has been obtained from much more data than we use for v_{term}). Clearly, the W_i are subject to ones prejudices, we took $W_{\text{in}} = W_{\text{out}} = W_{\text{other}} = N_{\text{other}} = 6$.

There are contributions to χ_{in}^2 from 53 data points at $l < 0$ and 77 at $l > 0$. In order to minimize the influence of systematic deviations from circular motion, which differ on the two sides of the Galaxy,

the data for positive and negative longitude are weighted by 0.844 and 1.23, respectively. This gives an effective number of 65 data points on either side, while leaving the effective total number of data points unchanged. In order to allow for non-circular motions both random and systematic, we adopt a constant uncertainty of $7\,\text{km s}^{-1}$ for v_{term}. Hence each data point adds to χ_{in}^2 an amount

$$w\left(\frac{v_{\text{term,model}}(l) - v_{\text{term,data}}(l)}{7\,\text{km s}^{-1}}\right)^2 \quad (21)$$

where $w = 0.844$ or $w = 1.23$ depending on whether l is greater than or less than 0.

The rotation-curve data for $R > R_0$ cannot be treated in an exactly analogous way because now two numbers contain significant uncertainties: d and W. Following Fich, Blitz & Stark (1989) we take the contribution to χ^2 from the ith data point to be

$$w\min_{R>R_0}\left\{\left[\frac{\ln d_i - \ln d_{\text{model}}(R)}{\Delta \ln d_i}\right]^2 + \left[\frac{W_i - W_{\text{model}}(R)}{\Delta W_i}\right]^2\right\}, \quad (22)$$

where $\Delta \ln d$ and ΔW are the uncertainties in the observables. In order to give each catalog the same weight, the data taken from Brand & Blitz (1993) and Pont et al. (1997) are weighted by $w = 0.665$ and 2.016, respectively, leaving the effective total number of data points unchanged at 119. To account for non-circular motions, a dispersion velocity of $7\,\text{km s}^{-1}$ is quadratically added to the measurement errors of v_{lsr}.

5 RESULTS

There are two aspects of any given model to consider: (i) how well does it fit the observational constraints, and (ii) how is its mass distributed. Since the observational constraints mostly relate to motions in the plane, these two questions are in large degree independent of one another. Table 3 lists the defining characteristics of each model and the quality of the fit to the data that it furnishes. Table 4 lists the values of each model's parameters.

The most important parameter of the models proves to be $R_{\text{d},*}/R_0$. The first four rows of Tables 3 and 4 refer to our 'standard models', which all have $R_0 = 8$ kpc but adopt four values of $R_{\text{d},*}/R_0$: 0.25, 0.3, 0.35 and 0.4. Each model is determined by specifying the value of $R_{\text{d},*}/R_0$ and then solving for the values of the other model parameters which minimize χ_{tot}^2. These values are given in Table 4.

Fig. 2 shows the circular-speed curves predicted by the four standard models together with the contributions to v_c from each component. In all four models the circular speed declines outside R_0, although in Model 4 the decline is extremely slow near R_0.

As $R_{\text{d},*}/R_0$ increases from 0.25 to 0.4, the peak in the contribution of the disc to v_c moves outwards from 5 kpc and the amplitude of the contribution of the disc to v_c declines markedly. This decline in the contribution of the disc to the inner circular-speed curve is compensated by an increase in the contribution of the halo. This increase is achieved by making the halo more centrally concentrated, with the result that for $R_{\text{d},*}/R_0 \gtrsim 0.35$ the halo does not differ greatly from a pure power-law component, the contribution of which to v_c is nearly independent of radius. For $R_{\text{d},*}/R_0 = 0.4$ this contribution dominates v_c at *all* radii.

The parameter $\Sigma_{\text{d,tot}}$ is the sum of the values for the three discs of the parameter Σ_{d} that is defined by equation (1). Table 4 shows that $\Sigma_{\text{d,tot}}$ decreases by a factor of almost 4 as $R_{\text{d},*}/R_0$ increases from 0.25 to 0.4. Consequently, the contribution of the disc to v_c at small radii decreases by a factor of 2, which is first compensated by a near doubling in the bulge mass, and then by a dramatic increase in the central density of the halo. Specifically, whereas for the smallest

Table 3. Fit results.

Model	$\frac{R_{d,*}}{R_0}$	Deviations from standard	Σ_0	A	B	$v_c(R_0)$	$\frac{K_{z,1.1}}{2\pi G}$	$M_{R<100\text{kpc}}$	σ_{BW}	χ^2_{in}	χ^2_{out}	χ^2_{other}	χ^2_{tot}
1	0.25	–	43.3	14.4	−13.3	222	68.0	6.56×10^{11}	100	91.2	174	1.92	13.9
2	0.30	–	52.1	14.3	−12.9	217	72.2	6.52×10^{11}	108	82.3	171	0.53	12.2
3	0.35	–	52.7	14.1	−13.1	217	72.5	6.51×10^{11}	111	86.7	175	0.46	12.5
4	0.40	–	50.7	13.8	−13.6	220	72.1	6.04×10^{11}	111	93.7	180	0.94	13.5
2a	0.30	$R_0 = 7.5$ kpc	52.5	15.1	−12.2	204	71.3	6.95×10^{11}	106	83.5	164	0.70	12.1
2b	0.30	$R_0 = 8.5$ kpc	50.3	13.8	−13.3	231	71.9	6.33×10^{11}	108	81.0	176	0.87	12.7
2c	0.30	$\gamma_h = 1$	52.3	14.3	−12.7	216	72.0	6.77×10^{11}	105	83.9	171	0.69	12.4
2d	0.30	$\gamma_h = 1$ and $\beta_h = 3$	53.3	14.2	−12.9	217	72.9	6.33×10^{11}	108	84.3	176	0.66	12.7
2e	0.30	$0.1\cos R/R_d$ added to exponent in (1)	49.6	14.3	−13.0	218	71.3	6.49×10^{11}	105	85.5	176	0.78	12.8
2f	0.30	$-0.1\cos R/R_d$ added to exponent in (1)	52.8	14.4	−12.6	217	72.0	6.77×10^{11}	108	80.6	166	0.42	11.8
2g	0.30	constraint $\sigma_{BW} = 140 \pm 15\,\text{km s}^{-1}$	51.4	14.1	−13.2	218	72.0	6.39×10^{11}	115	95.1	176	2.99	15.1
2h	0.30	$M_b \geq 1.5\times10^{10}\,M_\odot$	44.1	13.9	−14.0	223	68.5	6.01×10^{11}	124	131	181	1.71	15.9
2i	0.30	halo axis ratio $q_h = 0.3$	40.0	14.0	−11.9	207	77.9	5.59×10^{11}	109	88.8	187	2.68	15.1
4a	0.40	$R_0 = 7.5$ kpc	49.6	14.3	−13.6	210	71.5	5.43×10^{11}	116	103	175	1.16	13.9
4b	0.40	$R_0 = 8.5$ kpc	50.8	13.4	−13.7	231	72.4	6.29×10^{11}	107	89.1	186	1.50	14.1
4c	0.40	$\gamma_h = 1$	49.8	13.9	−13.7	221	71.9	5.75×10^{11}	106	92.1	178	1.48	13.8
4d	0.40	$\gamma_h = 1$ and $\beta_h = 3$	48.3	14.0	−13.8	222	71.4	3.73×10^{11}	107	89.6	173	2.99	14.7
4e	0.40	$0.1\cos R/R_d$ added to exponent in (1)	51.7	14.0	−13.3	218	72.5	6.36×10^{11}	111	88.6	179	0.57	12.9
4d	0.40	$-0.1\cos R/R_d$ added to exponent in (1)	49.5	13.7	−13.9	221	71.7	5.76×10^{11}	110	99.1	182	1.41	14.2
4g	0.40	constraint $\sigma_{BW} = 140 \pm 15\,\text{km s}^{-1}$	52.0	13.8	−13.4	218	72.4	6.27×10^{11}	117	106	182	2.87	15.8
4h	0.40	$M_b \geq 1.5\times10^{10}\,M_\odot$	48.3	13.7	−14.2	223	71.5	4.89×10^{11}	120	114	181	2.06	15.5
4i	0.40	halo axis ratio $q_h = 0.3$	40.0	13.6	−12.3	207	80.2	3.41×10^{11}	112	105	197	5.57	18.7

The standard models 1 to 4 are determined by the choice of $R_{d,*}/R_0$ (column 3), where $R_0 = 8$ kpc. The non-standard models 2a–i and 4a–i are specified in column 4. Columns 5 to 11 give the best-fitting values of the observables discussed in Section 3.3. The values obtained for the χ^2s defined in Section 4 are given in the last four columns. The units are as usual: R_0 in kpc; Σ_0, $K_{z,1.1}/(2\pi G)$ in $M_\odot$ pc^{-2}; A, B in km s^{-1}kpc^{-1}; $M_{R<100\text{kpc}}$ in $M_\odot$; and $v_c(R_0)$ and σ_{BW} in km s^{-1}.

Table 4. Best-fitting values of the model parameters.

Model	$\Sigma_{d,tot}$	$\rho_{0,b}$	$\rho_{0,h}$	γ_h	β_h	$r_{0,h}$	$r_{t,h}$	M_d	M_b	$M_{h,<10\text{kpc}}$	$M_{h,<100\text{kpc}}$
1	1905	0.4271	0.7110	−2	2.959	3.83	∞	5.13	0.518	2.81	60.0
2	1208	0.7561	1.263	−2	2.207	1.09	∞	4.88	0.917	2.89	59.4
3	778.4	0.3	0.1179	1.8	2.002	2.29	∞	4.46	0.364	4.36	60.3
4	536	0.3	0.2659	1.629	2.167	1.899	∞	4.16	0.364	5.23	55.9
2a	1222	0.3958	0.0009166	1.8	1.634	22.79	∞	4.32	0.48	2.46	64.7
2b	1165	0.7874	1.425	−2	2.553	1.733	∞	5.32	0.955	4	57.1
2c	1213	0.5995	0.03055	1	2.209	6.185	∞	4.9	0.727	2.99	62.1
2d	1238	0.6754	0.006159	1	3	21.8	∞	5	0.819	2.83	57.5
2e	1260	0.6584	0.9084	−2	2.425	1.802	∞	5.04	0.798	2.88	59
2f	1121	0.3	0.4179	1.8	1.888	1	∞	4.6	0.364	3.7	62.7
2g	1193	0.953	0.8326	−2	2.447	1.919	∞	4.82	1.16	2.77	57.9
2h	1024	1.237	1.071	−2	2.888	2.877	∞	4.13	1.5	3.4	54.5
2i	928.2	0.3380	0.8514	1.8	1.868	1	∞	3.75	0.41	2.92	51.7
4a	526.5	0.3	0.7555	1.757	2.108	1	∞	3.59	0.364	4.43	50.4
4b	534.9	0.3	0.05205	1.556	2.386	5.239	∞	4.7	0.364	6.26	57.8
4c	527	0.4147	1.293	1	2.233	1	∞	4.09	0.503	5.21	52.9
4d	511	0.6507	0.1101	1	3	5.236	∞	3.97	0.789	5.13	32.5
4e	584	0.3	0.1078	1.764	2.076	2.628	∞	4.45	0.364	4.74	58.8
4f	491.3	0.3	0.3926	1.5	2.256	1.764	∞	3.91	0.364	5.66	53.4
4g	549.6	0.3	0.7447	1.8	2.066	1	∞	4.27	0.364	5.04	58.1
4h	510.6	1.237	3.313	−2	2.672	1.262	∞	3.97	1.5	4.44	43.4
4i	423	0.3	2.799	1.282	2.336	1	∞	3.29	0.364	3.95	30.5

Columns 2 to 8 give the values of the parameters obtained from the fitting procedure; surface and volume densities are given in $M_\odot$ pc^{-2} and $M_\odot$ pc^{-3} respectively. The last four columns give, in units of $10^{10}\,M_\odot$, the total masses of disc and bulge, and the mass of the halo within 10 and 100 kpc.
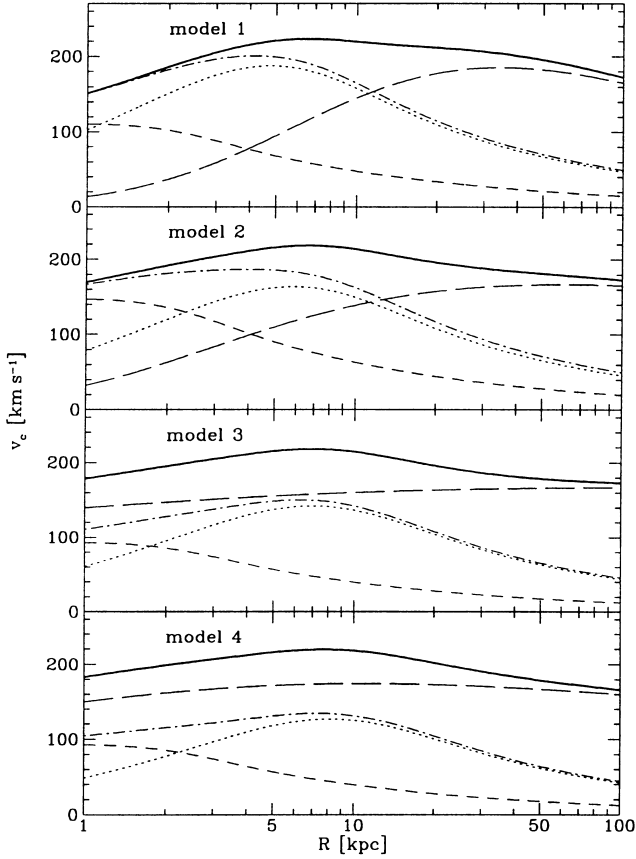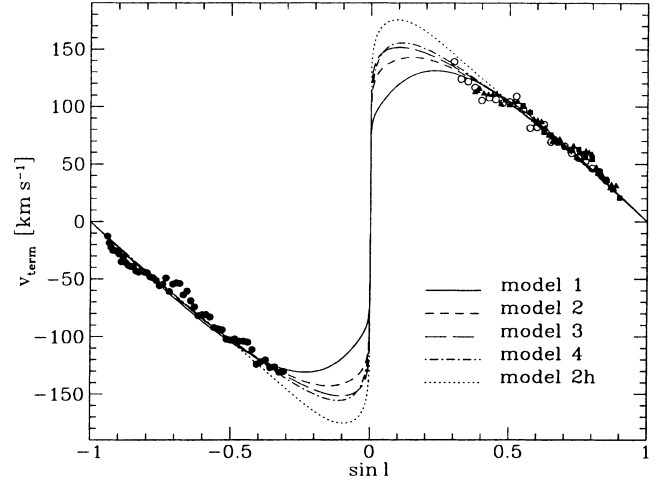
Figure 2. Rotation curves of models 1–4 (thick solid lines). The circular velocities owing to the disc (dotted lines), bulge (short-dashed lines), disc and bulge (dash–dotted lines), and halo (long-dashed lines) are also shown.

Figure 3. Terminal velocities at $R \lesssim R_0$ for models 1–4 and 2h. The data are from Weaver & Williams (1974, filled triangles), Bania & Lockman (1984, filled squares), Knapp et al.(1985, open circles), and Kerr et al.(1986, filled circles).

Figure 4. W (equation 11) versus R/R_0 for models 1–4 (hard to distinguish) and the two most extreme models 2b,i. The data are from Brand & Blitz (1993; triangles) and Pont et al. (1997; dots).

two values of $R_{\mathrm{d},*}/R_0$ the halo has a hole at its centre ($\gamma_\mathrm{h} = -2$), for all larger values of $R_{\mathrm{d},*}/R_0$ the halo density decreases outwards as $\sim r^{-1.7}$.
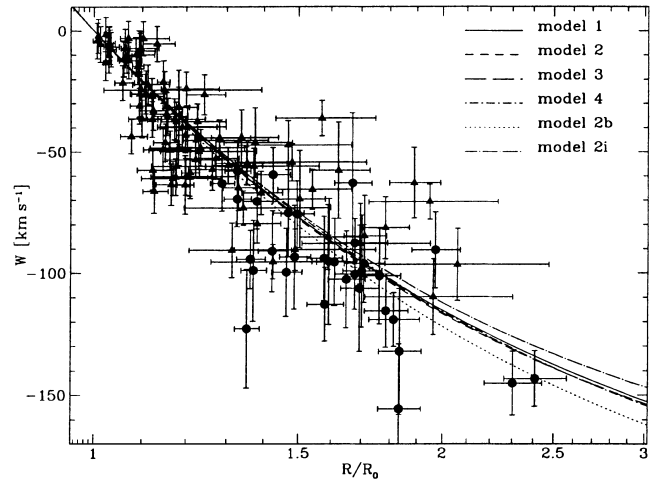
The amplitude of the contribution of the bulge to v_c near the centre is largest for $R_{\mathrm{d},*}/R_0 = 0.3$ – smaller and larger values of this parameter yield bulges that are less massive by a factor in excess of 40 per cent. In all four models the velocity dispersion in Baade's window lies below the target value. As we indicated above, this shortfall probably reflects the fact that our models take no account of the elongation of the bulge along the line of sight.

The model with the smallest value of $R_{\mathrm{d},*}/R_0$ is nearly a maximum-disc model in the sense that there is a wide range of radii $R \lesssim 10\,\mathrm{kpc}$ within which nearly all of v_c derives from the disc alone. In Model 2, which has $R_{\mathrm{d},*}/R_0 = 0.3$, the disc and bulge together dominate v_c at $R \lesssim 10\,\mathrm{kpc}$; the principal difference between Models 1 and 2 is the dominance of the bulge at $R \lesssim 2\,\mathrm{kpc}$ discussed above. For $R_{\mathrm{d},*}/R_0 \gtrsim 0.35$ the contribution of the disc to v_c is nowhere as important as the halo, even though the discs of these models are only slightly less massive than those of models with $R_{\mathrm{d},*}/R_0 \lesssim 0.3$.

All the standard models have masses $M_{R<100\mathrm{kpc}}$ that lie below the target value. This is because the rotation-curve data for $R > R_0$ force v_c to decline just beyond the Sun. In extreme cases – for example Model 3 and Model 2a below – the constraint on $M_{R<100\mathrm{kpc}}$ obliges the halo to make an outwards-increasing contribution to v_c even at the largest radii, with the result that v_c is increasing at $R = 100\,\mathrm{kpc}$.

All four standard models provide satisfactory fits to the constraints of Section 3.3 – see Table 3. Fig. 3 shows that these models also provide excellent fits to the observed tangent velocities at $R < R_0$: the deviations between observed and predicted points are of the order of those expected to arise from spiral structure. Fig. 4 shows that all four standard models provide essentially the same reasonable fit to the (widely scattered) rotation-curve data for $R > R_0$.

Tables 3 and 4 also describe variants of the standard models. Models 2a and 2b explore the effect of changing R_0: reducing R_0 from 8 to 7.5 kpc increases A and reduces $v_\mathrm{c}(R_0)$. The top two panels of Fig. 5 show that it also changes the form of $v_\mathrm{c}(R)$ from steady decline at all $R > R_0$ to a steady rise at $R \gtrsim 40\,\mathrm{kpc}$. This coupling between the value of R_0 and the rotation curve at $R \gg R_0$ arises because the tangent velocities strongly constrain the mass distribution at $R < R_0$. Hence any change in one component at
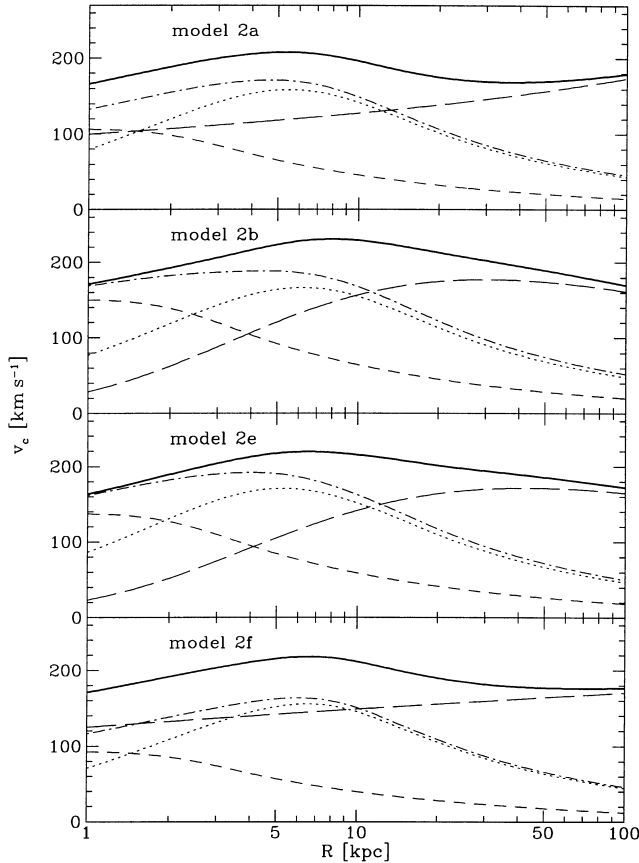
Figure 5. Rotation curves of models 2a,b,e,f (thick solid lines). The circular velocities owing to the disc (dotted lines), bulge (short-dashed), disc and bulge (dash-dotted lines), and halo (long-dashed lines) are also shown.

$R < R_0$ must be compensated by a change in another component. Since our model for the halo has only a few free parameters, a change in its density at $R < R_0$ is accompanied by significant changes in density at $R \gg R_0$, and vice versa.

Model 2c shows the effect of fixing the inner slope of the density profile of the halo at $\gamma_h = 1$; this value is motivated by Navarro, Frenk & White (1996), who find that in simulations of cosmological clustering, dark-matter haloes tend to a universal profile that has a slope ~ 1 at small radii. Even though Model 2 has $\gamma_h = -2$, fixing γ_h in this way has a negligible effect on the observable properties of the model, and causes a negligible increase in χ^2_{tot}. This is because the halo makes a negligible contribution to the central density even for $\gamma_h = 1$. Moreover, the increase in γ_h is at small radii largely compensated for by a six-fold increase in the break radius $r_{0,h}$ of the halo.

Model 2d explores the effect of fixing both the inner and the outer slopes of the halo to values, $\gamma_h = 1, \beta_h = 3$, that are suggested by Navarro et al. (1996). Again the observables of the model and value of χ^2_{tot} change remarkably little, while $r_{0,h}$ increases again, this time by a further factor of ~ 3.

Models 2e and 2f show the effect of employing a slightly non-exponential disc: a term $\pm 0.1 \cos(R/R_d)$ is added to the exponent in equation (1). The lower two panels of Fig. 5 show that at $R \lesssim 10$ kpc this extra term changes the balance between the contributions to v_c of the bulge, disc and halo without significantly affecting the overall rotation curve. At large R the effect of the additional term is more dramatic in that with a plus sign v_c declines steadily at $R > R_0$,

while with a minus sign it rises gently at the largest radii. Again we encounter the consequence of the rotation curve at large radii being inadequately constrained by the observations: it mirrors changes in the functional form of the halo that are designed to fit the data at $R \lesssim R_0$.

Model 2g shows that increasing σ_{BW}, the target dispersion in Baade's window, by 23 km s^{-1} has little effects on the derived model: the predicted dispersion is grudgingly raised from 108 to 115 km s^{-1}, and χ^2_{tot} increases significantly.

Microlensing surveys have suggested that the bulge may be significantly more massive than studies of the tangent velocities would imply (e.g., Bissantz et al. 1997). Model 2h shows the effect of imposing the constraint $M_{bulge} \geq 1.5 \times 10^{10}$ M$_\odot$. This causes v_c to be dominated by the bulge out to ~ 3.5 kpc. It also, by the mechanism described above, changes the form of $v_c(R)$ at large R so that with a more massive bulge v_c is predicted to decline significantly more steeply at $R \gtrsim 50$ kpc. Like the other model with an artificially enhanced bulge (Model 2g), this model has an anomalously large value of χ^2_{tot}.

It is not clear that a massive halo should be nearly round (axial ratio $q_h = 0.8$) as in all the models described above, so Model 2i explores the effect of assuming that the halo is highly flattened: axial ratio $q_h = 0.3$. This has the effect of making the halo virtually a pure power-law component that is dynamicaly dominant at all radii. Consequently, it predicts that the rotation curve rises at the very largest radii. The massive, flattened halo contributes strongly to $K_{z,1.1}$, so that the target value of $K_{z,1.1}$ is significantly overshot, despite the local disc surface density, Σ_0, being pushed right down to its floor value, $\Sigma_0 = 40$ M$_\odot$ pc^{-2}. For this model χ^2_{tot} is on the high side.

Models 4a–i explore the effect on Model 4 of the changes that were made to Model 2 in making Models 2a–i. Qualitatively the results are similar, but quantitatively they tend to be smaller because the halo is very much more important in Model 4 than it is in Model 2 and the effects of changes in the disc and bulge are relatively minor.

Inspection of Table 4 shows that there is a general anticorrelation between the steepness of the central density profile of the halo and the bulge mass. In particular, when the halo density is strongly cusped at the centre ($\gamma_h > 1$), the bulge mass is small: $M_b \sim 0.37 \times 10^{10}$ M$_\odot$. Conversely, with the exception of the model with the smallest value of $R_{d,*}/R_0$, the bulge mass is large ($M_b \gtrsim 0.8 \times 10^{10}$ M$_\odot$) when the halo has a hole at its centre ($\gamma_h = -2$).

The asymptotic slope of the halo profile at large R is always larger than $\beta_h = 1.63$ and no model has a finite halo cut-off radius $r_{t,h}$. That is, the data imply only that the halo ends at $R > 100$ kpc.

The only models that comes near to violating the lower limit (17) on the local column density are Model 1, which has the smallest disc scalelength, Model 2h, which is obliged to have a massive bulge, and Models 2i and 4i, which have highly flattened haloes.

Table 5 gives the correlation matrix of the fitted parameters for both Models 2 and 4: the upper right triangle is for Model 2 while the lower-left triangle is for Model 4. The parameters of the halo are strongly correlated with one another. Indeed, the density normalization of the halo $\rho_{0,h}$, central slope γ_h and scalelength $r_{0,h}$ have almost unit correlations between them. The density normalization of the bulge, $\rho_{0,b}$ is strongly correlated with all the halo parameters, especially $\rho_{0,h}$, γ_h and $r_{0,h}$. By contrast, $\Sigma_{d,tot}$ is only weakly correlated with the other parameters. These strong correlations between parameters reflect the existence of a long, level valley in parameter space.

Table 5. Parameter correlations for models 2 (upper right) and 4 (lower left).

	$\rho_{0,h}$	γ_h	β_h	$r_{0,h}$	$r_{t,h}$	$\rho_{0,b}$	$\Sigma_{d,tot}$
$\rho_{0,h}$	-	−0.999	−0.953	−0.999	−0.909	0.917	−0.161
γ_h	−0.714	-	0.952	0.998	0.907	−0.920	0.153
β_h	−0.990	0.646	-	0.968	0.989	−0.788	0.112
$r_{0,h}$	−0.999	0.705	0.992	-	0.929	−0.900	0.153
$r_{t,h}$	−0.963	0.643	0.984	0.965	-	−0.729	0.109
$\rho_{0,b}$	−0.877	0.312	0.891	0.882	0.846	-	−0.175
$\Sigma_{d,tot}$	0.089	−0.126	−0.061	−0.089	−0.005	−0.013	-

6 CONCLUSIONS

We have fitted a multiparameter mass model to the available kinematic data for the Milky Way. The wide variety of models that emerge from this fitting process demonstrates that the mass distribution within the Milky Way is currently ill determined.

The principal problem in determining the mass distribution of the Galaxy is that very few hard facts are available regarding the vertical distribution of the Galaxy's mass. Also the circular speed is observationally much less well constrained at $R > R_0$ than it is at $R < R_0$. These deficiencies in the spatial coverage of the data have several unfortunate effects. First they oblige use to represent the Galaxy as a superposition of components, and to adopt simple functional forms for the distribution of mass within each component.

The assumed distribution of mass within the halo plays a particularly important and confusing role. Since we know nothing about the halo except what can be gleaned from studies such as this, we have allowed the halo density as much freedom as is compatible with (i) its being much thicker than the disc (axial ratio $q_h \geq= 0.3$), (ii) its density function containing only a few free parameters, and (iii) its not being implausibly sharp-edged ($-2 \leq \gamma_h \leq 1$, $\beta_h \geq 1$).

With these assumptions we find that even the circular-speed curve of the best-fitting model depends significantly on both the adopted values of parameters such as $R_{d,*}/R_0$ and R_0, and on the adopted functional forms of the components. The density model is even less well constrained by the data. In particular, remarkably small changes in $v_c(R)$ and the other observational constraints can be associated with dramatic changes in the distribution of mass between the different components, and the degree of central concentration of the halo.

A particularly disturbing phenomenon is that a change in a component that contributes to v_c only at small radii causes the predicted value of v_c to change at large radii. This connection between small and large scales within the Galaxy is established by the halo component, which must be allowed to contribute to the density at all radii and yet be determined by a small number of parameters. In general there is a clear need to model components non-parametrically or at least by functions that contain more parameters. However, we do not yet have enough observational constraints to constrain adequately models that are significantly more complex than those used here.

As is traditional, we have represented the Galaxy as a superposition of components that individually represent plausible stellar systems. The justification for the use of such components in preference to a family of orthogonal (and therefore non-positive) functions, is the hypothesis that these components do, in fact, represent real physical systems. While there can be no doubt of the reality of the disc and bulge, the status of the halo is entirely speculative. Indeed, although observations of external galaxies

clearly require high mass-to-light ratios at large radii, it does not follow that these reflect the existence of a physically distinct dark halo; it is perfectly possible that the mass-to-light ratio of the disc or bulge increases strongly away from the Galactic Centre. If the halo does represent a distinct dynamical entity, then in an exercise like the present one it should emerge with a dynamically plausible density profile. Table 4 shows that it frequently fails this test: in just over half the models, the central density slope γ_h lies at one or other extreme of its permitted range $-2 \leq \gamma_h \leq 1.8$. In four models (Models 3, 2a, f,i) the density profile of the halo is an essentially featureless power law of slope ~ -1.8. In seven models the halo has a hole at its centre. *N*-body simulations of structure formation offer no encouragement to the idea that the Galaxy's distribution of axions or other exotic particles would have a hole at its centre. Nor do they suggest that it should be a featureless power law (Navarro et al. 1996).

The road to an improved understanding of the mass distribution of the Galaxy must lie with the introduction of more observational constraints, especially ones that relate to $R > R_0$ and $z \gtrsim R$. The goal of later papers in this series is to bring to bear on this problem observations of halo stars, which should provide a wealth of information about the density at $z \gtrsim R$, and, to a lesser extent, about the density at $R > R_0$. The models described here simultaneously provide starting points for this enterprise and demonstrate its urgency by underlining that at the present time we know depressingly little about the distribution of mass within our own Galaxy.

REFERENCES

Backer C. D., 1996, in Blitz L., Teuben P., eds, Proc. IAU Symp. 169, Unsolved Problems of the Milky Way. Kluwer, Dordrecht, p. 193
Bahcall J. N., Soneira R. M., 1980, ApJS, 44, 73
Bania T. M., Lockman F. J., 1984, ApJS, 54, 513
Binney J. J., 1994, in Morrison L. V., Gilmore G. F., eds, Galactic and Solar System Optical Astrometry. Cambridge Univ. Press, p. 141
Binney J. J., Gerhard O. E., Spergel D. N., 1997, MNRAS, 288, 365
Binney J. J., Tremaine S., 1987, Galactic Dynamics. Princeton Univ. Press, Princeton
Bissantz N., Englmaier P., Binney J. J., Gerhard O. E., 1997, MNRAS, 289, 651
Brand J., Blitz L., 1993, A&A, 275, 67
Caldwell J. A. R., Ostriker J. P., 1981, ApJ, 251, 61
Cowsik R., Ratnam C., Bhattacharjee P., 1996, Phys. Rev. Lett., 76, 3886
Dame T. et al., 1987, ApJ, 322, 706
Dehnen W., Binney J. J., 1996, in Morrison H., Sarajedini A., eds, ASP Conf. Ser. 92. Formation of the Galactic Halo ... Inside and Out. Astron. Soc. Pac., San Francisco p. 393
Eckart A., Genzel R., 1997, MNRAS, 284, 576
Evans N. W., 1996, Phys. Rev. Lett., submitted
Feast M. W., Catchpole R. M., 1997, MNRAS, 286, L1
Feast M. W., Whitelock P. A., 1997, MNRAS, 291, 683
Fich M., Blitz L., Stark A. A., 1989, ApJ, 342, 272
Gates E. I., Gyuk G., Turner M. S., 1995, ApJ, 449, L123
Gould A., Ramírez S. V., 1997, preprint (astro-ph/9705174)
Hanson R. B., 1987, AJ, 94, 409
Kerr F. J., Lynden-Bell D., 1986, MNRAS, 221, 1023
Kerr F. J., Bowers P. F., Jackson P. D., Kerr M., 1986, A& AS, 66, 373
Knapp G. R., Stark A. A., Wilson R. W., 1985, AJ, 90, 254
Kochanek C. S., 1996, ApJ, 457, 228
Kuijken K., Dubinski J., 1994, MNRAS, 269, 13
Kuijken K., Gilmore G., 1989, MNRAS, 239, 605
Kuijken K., Gilmore G., 1991, ApJ, 367, L9
Laney C. D., Stobie R. S., 1994, MNRAS, 266, 441
Lin D. N. C., Jones B. F., Klemola A. R., 1995, ApJ, 439, 652

Malhotra S., 1994, ApJ, 433, 687

Malhotra S., 1995, ApJ, 448, 138

Merrifield M. R., 1992, AJ, 103, 1552

Navarro J., Frenk C. S., White S. D. M., 1996, ApJ, 462, 563

Olling R. P., 1996, AJ, 112, 4810

Oort J. H., 1932, Publ. Astron. Inst. Neth. 6, 349

Pont F., Queloz D., Bratschi P., Mayor M., 1997, A&A, 318, 416

Rich R. M., 1988, AJ, 9, 5 828

Rohlfs K., Kreitschmann J., 1988, A&A, 201, 51

Sackett P. D., Rix, H-W., Jarvis B. J., Freeman K. C., 1994, ApJ, 436, 629

Schmidt, M., 1956, Bull. Astr. Inst. Neth., 13, 15

Sciama D. W., 1990, ApJ, 364, 549

Terndrup D. M., Sadler E. M., Rich R. M., 1995, AJ, 110, 1774

Weaver H., Williams D. R., 1974, A&AS, 17, 1

This paper has been typeset from a T$_E$X/L^{A}T$_E$X file prepared by the author.